universe

MDPI

*Article*

# Flux Rope Eruption and Associated Vertical Prominence Oscillation

**Yanjie Zhang * and Qingmin Zhang**

Purple Mountain Observatory, Chinese Academy of Sciences, Nanjing 210023, China; zhangqm@pmo.ac.cn
* Correspondence: zhangyj@pmo.ac.cn

**Abstract**

We present a plane-of-sky observational analysis of a solar eruptive event that occurred on 2 September 2023. The flare peaked at approximately 07:00 UT, closely aligning with the impulsive acceleration phase of the erupting flux rope, which accelerated from an initial speed of 42 km $s^{-1}$ to 501 km $s^{-1}$. The associated coronal mass ejection (CME) propagated through interplanetary space at a near-constant speed of 519 km $s^{-1}$, suggesting that its kinetic energy was primarily acquired within the lower solar atmosphere. Comparison of the projected propagation directions of the erupting flux rope and the CME reveals an apparent angular offset of approximately 10°, which is interpreted through Potential Field Source Surface (PFSS) modeling as the result of asymmetric magnetic pressure gradients. Notably, the overlying coronal loops exhibited a piecewise acceleration, with the velocity increasing from approximately 7 km $s^{-1}$ to 320 km $s^{-1}$. Furthermore, the passage of the eruption-induced disturbance triggered large-amplitude, damped vertical oscillations in an adjacent prominence. Applying magnetohydrodynamic (MHD) prominence seismology based on Hyder's model, we derive a local radial magnetic field strength of 1.77–7.02 G. These results provide a detailed view of the evolution from magnetic energy release to large-scale coronal disturbances and the subsequent prominence oscillation.

**Keywords:** Sun: activity; Sun: filaments, prominences; Sun: oscillations

## 1. Introduction

Solar eruptive events, encompassing flares, filament/prominence eruptions, and CMEs, are the most spectacular manifestations of magnetic energy release in the heliosphere [1–3]. The standard model [4–7] and its modern extensions [8,9] for solar eruptions typically involve the destabilization and subsequent eruption of stressed or twisted coronal magnetic fields—often in the form of magnetic flux ropes [10,11]—through magnetic reconnection or loss of equilibrium. Upon erupting into the upper corona, the flux rope stretches the overlying magnetic field lines, creating a highly elongated vertical current sheet behind it. This structural evolution triggers fast, explosive magnetic reconnection within the current sheet, establishing a powerful feedback that can significantly enhance the eruption and influence the subsequent evolution [12,13]. The reconnection processes efficiently convert the stored magnetic energy into thermal energy, kinetic energy, and particle acceleration. High-energy particle beams accelerated downward along the reconnected loops interact with the dense chromosphere, producing intense flare ribbons and subsequent post-flare loops observed across the electromagnetic spectrum [14]. At the same time, the reconnection injects new poloidal flux into the ascending core, providing a continuous MHD upward force that drives the plasma into interplanetary space as a CME.

Check for updates

Academic Editor: Costas Alissandrakis

Received: 8 July 2026
Revised: 21 September 2026
Accepted: 23 September 2026
Published: 28 September 2026

**Copyright:** © 2026 by the authors. Licensee MDPI, Basel, Switzerland. This article is an open access article distributed under the terms and conditions of the Creative Commons Attribution (CC BY) license.

Solar eruptions sometimes trigger large-scale global disturbances known as Extreme-Ultraviolet (EUV) waves [15,16]. Characterized by diffuse, expanding fronts propagating across the solar disk at typical speeds of 200–1000 km $s^{-1}$, the phenomena track the propagation of energy through the low corona [17]. While early literature debated whether EUV waves were flare-induced blast waves or non-wave geometric artifacts, modern high-cadence observations reveal a multi-component nature [18,19]. The prominent global EUV wave fronts are generally interpreted as fast-mode MHD waves, which may steepen into shocks under appropriate conditions and are often associated with the rapid lateral expansion of the CME flank [20]. However, not all EUV fronts necessarily correspond to freely propagating MHD waves; some may instead reflect CME-driven compression, magnetic-field-line stretching, or other non-wave restructuring of the corona [21]. Localized or secondary fronts can also result from interactions between the primary disturbance and structured coronal magnetic fields and have, in some cases, been interpreted as slow-mode MHD disturbances [22]. They provide a visible signature of the global coupling between the eruption and the surrounding coronal plasma and magnetic field.

When the propagating EUV waves impinge upon remote filaments/prominences, they act as an external mechanical driver that can trigger large-amplitude oscillations (LAOs) with velocity often exceeding 10 km $s^{-1}$ [23–28]. The impact of the incident wave front imparts a sudden pressure pulse or magnetic displacement to the prominence body, forcing the cool, dense plasma out of its magneto-hydrostatic equilibrium. Depending on the collision geometry and the orientation of the underlying magnetic skeleton, the impact excites either transverse oscillations restored by the Lorentz force [29–31], or longitudinal oscillations along the filament axis behaving similarly to a gravity-driven pendulum [32]. The subsequent damping and period of these wave-induced oscillations provide an exceptional diagnostic window for filament seismology, which can be utilized to indirectly deduce the magnetic field strength, shear angle, and local curvature of the filament channel [31].

In this paper, we present a comprehensive investigation of a solar eruption event that occurred on 2 September 2023 in NOAA active region (AR) 13413. The flare energetics, the kinematics of the erupting flux rope, the resulting EUV wave, and the prominence oscillation are detailed. We describe the data and method in Section 2. The results are presented in Section 3. The discussion and summary are given in Sections 4 and 5, respectively.

## 2. Data and Method

The event was captured by multi-instrument observations from the low corona to interplanetary space. EUV images from the Atmospheric Imaging Assembly (AIA; Lemen et al. [33]) on board the Solar Dynamics Observatory (SDO, Pesnell et al. [34]) were used to track the low-coronal evolution. Specifically, the AIA 131 Å channel, with a prominent response to hot plasma at approximately 10 MK as well as a cooler response component, was used to identify the hot-channel plasma. The 171 Å and 193 Å channels, with approximate dominant response temperatures of 0.6 MK and 1.6 MK, respectively, were used to study coronal loops and EUV disturbance propagation, while the 304 Å channel, with a dominant response near 0.05 MK, was utilized to track the cool prominence material. All data were log-transformed or subjected to base-difference processing.

Data from the Solar Orbiter (SolO; Müller et al. [35]) were also used. The Spectrometer/Telescope for Imaging X-rays (STIX, Krucker et al. [36]) provided hard X-ray light curves in four energy bands (4–10 keV, 10–15 keV, 15–25 keV, and 25–50 keV) to diagnose non-thermal and thermal flare energetics. Simultaneously, the Full Sun Imager (FSI) of the Extreme Ultraviolet Imager (EUI; Rochus et al. [37]) suite provided 174 Å observations from an off the Sun–Earth line perspective.

The Large Angle and Spectrometric Coronagraph (LASCO; Brueckner et al. [38]) on aboard SOHO and the Sun Earth Connection Coronal and Heliospheric Investigation (SECCHI; Howard et al. [39]) on STEREO-A provided white-light observations to track the CME into interplanetary space. Specifically, LASCO-C2 observes the corona over a range of 1.5–6.0 $R_\odot$ with a typical cadence of about 12 min, whereas STEREO-A/COR2 extends the field of view (FOV) to 15 $R_\odot$ with a cadence of about 15 min.

Repeated selection was performed on all manually picked points or segments to yield the mean value and/or uncertainty estimates.

## 3. Results

Figure 1a shows the relative positions of Earth, SolO, and the Sun on 2 September 2023 at 07:00 UT. In HEE coordinates, the heliocentric separation angle between SolO and Earth is 156°. Additionally, STEREO-A was located very close to the Earth, with an angular separation of 1.88° and a heliocentric distance of 0.96 AU. The eruption originated from AR 13413, which was located near the western limb as pointed by the black arrow. Figure 1b displays the AIA 131 Å observation at 06:54:30 UT, highlighting a bright, coherent, and non-radially erupting structure with a deviation angle of about 52° relative to the local radial vector, characteristic of a magnetic flux rope or hot channel. The white dashed line S0 represents the slit position used for the subsequent kinematic tracking. Figure 1c shows the co-temporal AIA 304 Å image with the same FOV, revealing two distinct chromospheric prominence structures, P1 and P2. P1 is located to the south of the eruption source at a relatively large distance, whereas P2 lies to the north of the source at a smaller distance. The white dashed lines S11, S12, S13 and S2 indicate the slits used to construct the time–distance diagrams of P1 and P2, respectively, with their orientation perpendicular to the prominence spine and the inferred magnetic field. Figure 1d shows the complementary FSI 174 Å image at 06:46:00 UT, revealing extensive coronal loop systems above the source region.

The eruption was accompanied by an M3.3 solar flare. Figure 2 illustrates the X-ray light curves recorded by STIX. The flux curves across all four energy bands (4–10 keV, 10–15 keV, 15–25 keV, and 25–50 keV) demonstrate an impulsive rise beginning around 06:35 UT. The curves reach their global peak at approximately 07:00 UT, before undergoing a typical gradual decay phase. The presence of significant emission in the higher energy bands (15–25 keV and 25–50 keV) points to substantial particle acceleration and non-thermal bremsstrahlung during the peak phase of magnetic reconnection.

The coronal response to the eruption can be evaluated by AIA 171 Å and 193 Å observations as shown in Figure 3. Panels (a1)–(a4) display a time series of AIA 171 Å images spanning the interval from 06:45:21 UT to 07:00:21 UT. The white dashed curves trace the rapid outward expansion of a series of overlying coronal loops, which are pushed ahead of the erupting flux rope. Simultaneously, a weak, propagating localized brightening moved along the solar disk. Panels (b1)–(b4) present four AIA 193 Å base-difference images, corresponding to four times at which the brightening signal is relatively pronounced, as indicated by the red arrow. Based on the relative positions and time intervals of the brightening, the projected velocity can be estimated at approximately $101.5 \pm 3.2$ km s$^{-1}$. It is worth noting that panel (b4) was observed at 07:00:16 UT, when the brightening was still some distance away from P1. Our subsequent study indicates that P1 began to oscillate at 06:52:45 UT. This temporal discrepancy suggests that the eruption-generated disturbance responsible for the onset of the P1 oscillation propagated through the corona ahead of the identifiable brightening. However, owing to its weak signal, the exact speed value could not be determined.

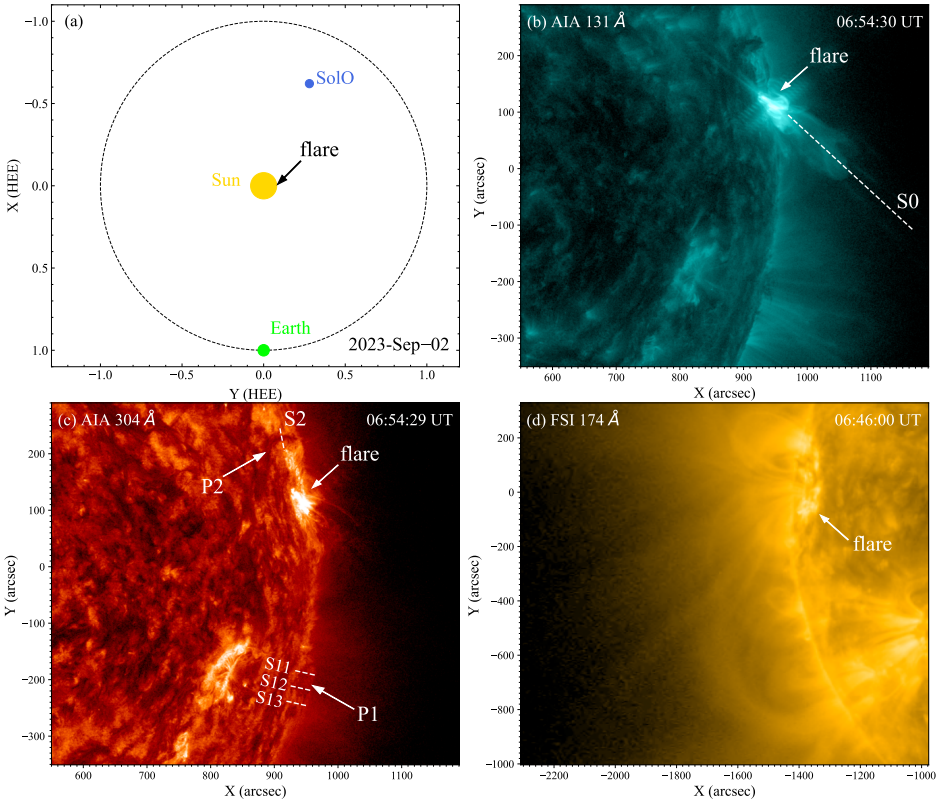



**Figure 1.** (**a**) Relative positions of Earth, SolO, and the Sun on 2 September 2023 at 07:00 UT in HEE coordinates. (**b**) AIA 131 Å image at 06:54:30 UT showing the erupting structure. The white dashed line S0 indicates the slit used for the subsequent kinematic analysis. (**c**) Co-temporal AIA 304 Å image with the same FOV, revealing two prominence structures, P1 and P2. The white dashed lines S11, S12, S13 and S2 are used to construct the time–distance diagrams of the prominence motions. (**d**) FSI 174 Å image at 06:46:00 UT, showing extensive coronal loop systems above the source region. (An animation of this figure is available in Supplementary Material).

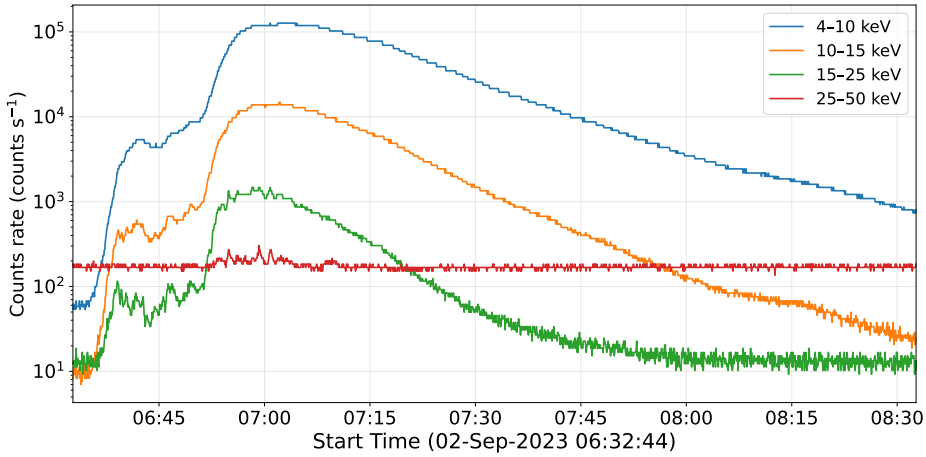



**Figure 2.** STIX X-ray count-rate light curves of the associated flare with the start time at 06:32:44 UT. The original data were accumulated in 4 s time bins and converted to count rates. No background subtraction was applied. All four energy bands (blue for 4–10 keV, orange for 10–15 keV, green for 15–25 keV, and red for 25–50 keV) exhibit a nearly synchronous impulsive rise beginning at approximately 06:35 UT, reaching a maximum around 07:00 UT, followed by a gradual decay phase. The light-travel-time difference between SolO and Earth-based instruments at this time is approximately 2 min 44 s.

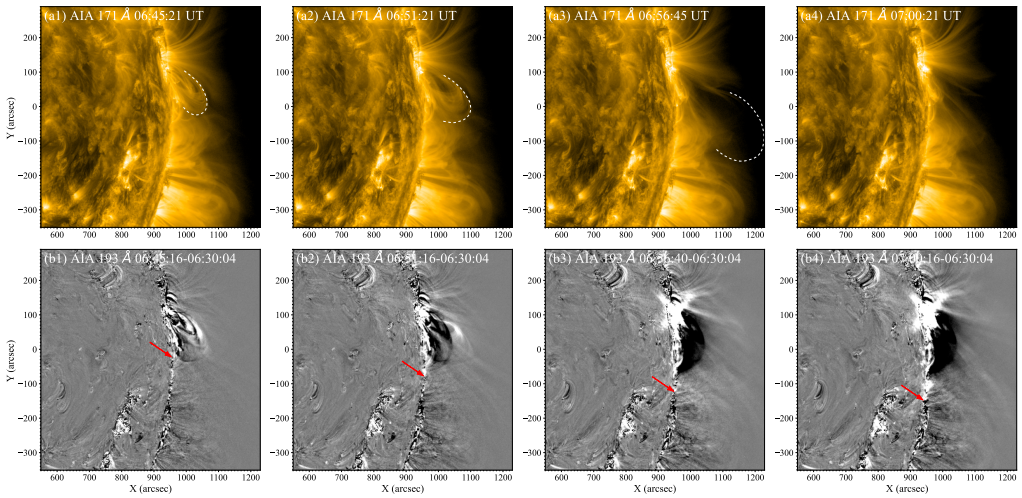



**Figure 3.** (**a1**)–(**a4**) A time sequence of AIA 171 Å images from 06:45:21 UT to 07:00:21 UT. The white dashed curves trace the rapid outward expansion of the overlying coronal loops. (**b1**)–(**b4**) The corresponding AIA 193 Å base-difference images, constructed by subtracting the base image at 06:30:04 UT. A propagating front of localized brightening is indicated by the red arrows.

Figure 4a presents the AIA 131 Å time-distance diagram of S0 from Figure 1b, which shows the trajectory of the erupting flux rope. Eight points (shown as red crosses) were manually selected along the leading edge of the coherent bright structure for trajectory fitting. In contrast to polynomial functions, the motion can be more adequately fitted by a combination of an exponential growth term, a linear term, and a constant term.

$$s(t) = c_0 e^{t/\sigma} + c_1 t + c_2 \quad (1)$$

where the parameter $\sigma$ represents the characteristic timescale over which the exponential component increases by a factor of e ($t$ starts at 0). It describes the rapid growth of the eruption velocity during the impulsive acceleration phase, rather than directly corresponding to a specific physical process. The uncertainties of the four parameters were also calculated using the nonlinear least-squares covariance matrix, as listed in Table 1.

The fit indicates an initial slow-rise phase, with a speed of 42 km s$^{-1}$ at 06:38:26 UT, followed by an impulsive acceleration that began at around 06:49:21 UT and increased the speed to 501 km s$^{-1}$ by 06:57:38 UT. The onset of the impulsive phase was defined as the time when the exponential component of the velocity becomes comparable to the linear component. And additional sensitivity tests were performed by varying the fitting interval and removing several manually selected points. The derived velocities remain within approximately 6%, demonstrating that the kinematic results are robust. This acceleration phase strongly correlates with the rising phase of the STIX X-ray light curves as shown in Figure 2, which is consistent with previous work [40].

Figure 4b presents the AIA 171 Å time–distance diagram along the same slit, illustrating the gradual uplift of coronal loops compressed by the erupting flux rope. The profile exhibits a multi-stage acceleration pattern, which is successfully fitted with a piecewise linear function. The fitted velocities are listed in Table 2, in which the uncertainties are calculated from the covariance matrix of the linear fit.

**Table 1.** The values and uncertainties of the parameters $c_0$, $\sigma$, $c_1$ and $c_2$.

| Parameter | $c_0$ (km) | $\sigma$ (s) | $c_1$ (km s$^{-1}$) | $c_2$ (km) |
|---|---|---|---|---|
| Value | 321.52 | 202.95 | 39.95 | 791.57 |
| Uncertainty | 20.42 | 15.61 | 2.83 | 10.57 |

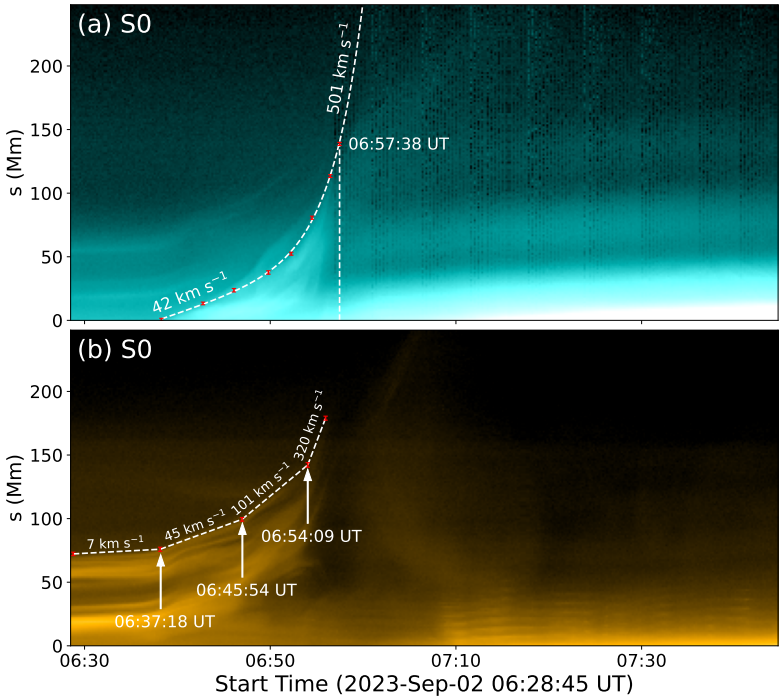



**Figure 4.** (**a**) AIA 131 Å time–distance diagram along S0 shown in Figure 1b. Red crosses mark the manually selected points, and the white dashed curve shows the best-fit function. (**b**) AIA 171 Å time–distance diagram along the same slit, showing the progressive uplift of overlying coronal loops. The white dashed lines denote the piecewise linear fit. The red error bars denote the manually selected points used for fitting, along with their uncertainties.

**Table 2.** Piecewise Velocities and Uncertainties of Coronal Loops Motion.

| Time Interval (UT) | Velocity (km s$^{-1}$) | Uncertainty (km s$^{-1}$) |
|---|---|---|
| 06:28:45–06:37:18 | 7 | 9 |
| 06:37:18–06:45:54 | 45 | 9 |
| 06:45:54–06:54:09 | 101 | 11 |
| 06:54:09–06:56:04 | 320 | 39 |

Following the passage of the eruption-driven disturbance, P1 was heavily disturbed and began oscillating. Figure 5a–c illustrate the time–distance diagram of P1 tracked along S11, S12, S13 in Figure 1c, respectively, with the red crosses denoting the manually selected fitting points. The prominence exhibited a distinct damped oscillatory motion, oriented perpendicular to the prominence spine after 06:52:45 UT. Due to the lack of spectroscopic data for measuring the line-of-sight (LOS) motion of the prominence, the perpendicular motion is defined in the plane of sky (POS). The trajectory was fitted using a classical damped sinusoidal function superimposed on a linear background drift:

$$s(t) = A_0 \sin\left(\frac{2\pi t}{P} + \Phi\right) e^{-t/\tau} + bt + y_0 \quad (2)$$

The best-fit parameters and their uncertainties obtained by bootstrap resampling are shown in Table 3. The similar periods and nearly coherent phases suggest that the oscillation is consistent with a kink-like vertical oscillation. In contrast, Figure 5d presents the time-distance diagram of P2 along S2. Despite being closer to the eruption region than P1, P2 exhibited no discernible POS disturbance and remained relatively stationary throughout the observation period.

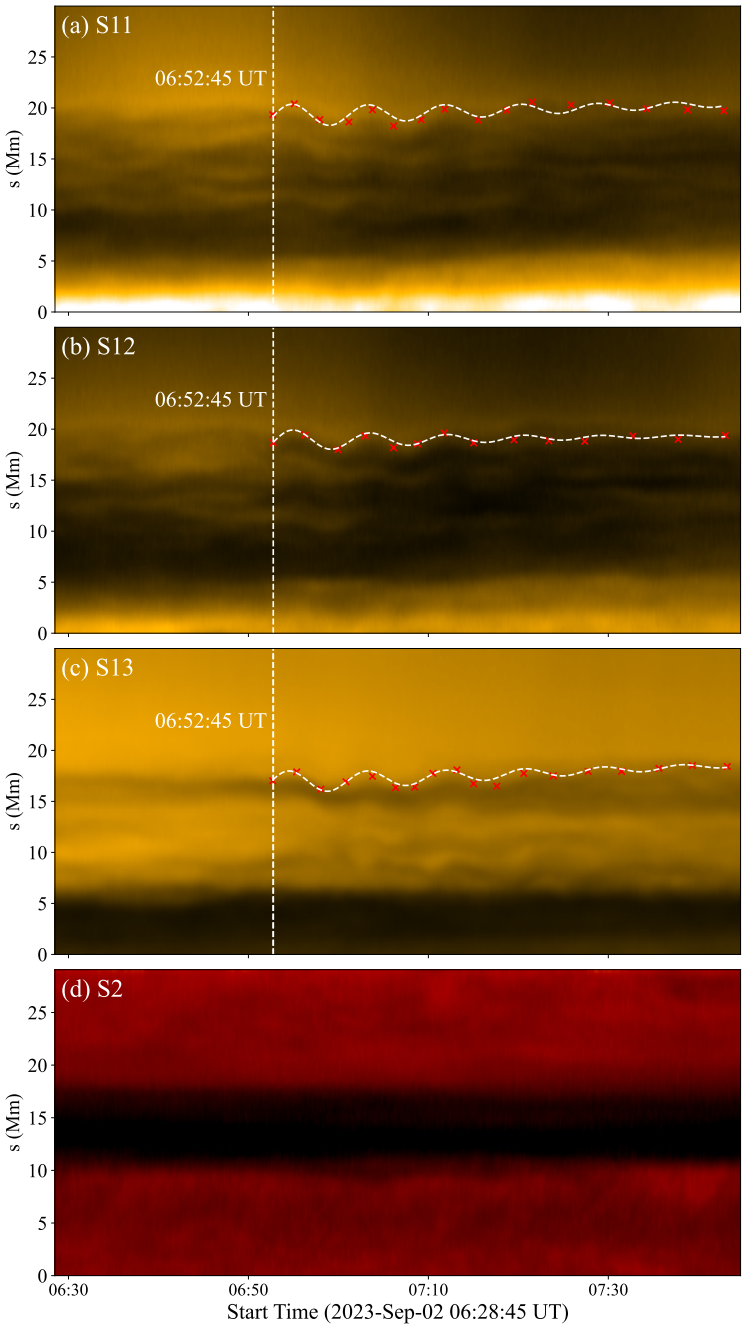



**Figure 5.** (**a**–**c**) Time–distance diagram of P1 along S11, S12 and S13 shown in Figure 1c, respectively. Red crosses indicate the fitting points, and the white dashed curve shows the damped sinusoidal fit. The vertical dashed line denotes the time at which P1 begins to exhibit pronounced oscillations. (**d**) Time–distance diagram of P2 along S2 shown in Figure 1c.

**Table 3.** Best-Fit Parameters of the P1 Oscillation and Comparison with Previous Studies of Prominence Oscillations.

| | $A_0$ (Mm) | $P$ (s) | $\Phi$ (rad) | $\tau$ (s) | $b$ (km s$^{-1}$) | $y_0$ (Mm) | $\tau/P$ | Classification | Geometry |
|---|---|---|---|---|---|---|---|---|---|
| S11 | $1.24 \pm 0.49$ | $509.43 \pm 10.68$ | $-0.03 \pm 0.32$ | $1983.85 \pm 227.43$ | $0.41 \pm 0.01$ | $19.03 \pm 0.26$ | 3.89 | Vertical | POS |
| S12 | $1.20 \pm 0.23$ | $514.37 \pm 9.01$ | $-0.09 \pm 0.15$ | $1200.80 \pm 270.94$ | $0.17 \pm 0.05$ | $18.70 \pm 0.32$ | 2.33 | Vertical | POS |
| S13 | $1.23 \pm 0.19$ | $524.50 \pm 7.73$ | $0.26 \pm 0.12$ | $1705.07 \pm 260.57$ | $0.58 \pm 0.06$ | $16.64 \pm 0.18$ | 3.25 | Vertical | POS |
| Event1 [41] | - | 793.65 | 3.02 | 1504.80 | - | - | 1.90 | Vertical | LOS |
| Event2 [42] | - | 660–1320 | - | 1500–3600 | - | - | 1.36–3.75 | Vertical | LOS |
| Event3 [43] | 16.08 | 1769.00 | 4.45 | 2639.96 | $-0.14$ | 52.38 | 1.49 | Transverse | 3D |

The erupting flux rope evolved into a prominent CME as it expanded into outer space, as shown in Figure 6. The CME exhibited a classical three-part morphology, characterized by a bright compact core embedded within a dark cavity and bounded externally by a bright leading front. Panels (a1)–(a4) show the STEREO-A/COR2 views from 07:23:30 UT to 10:23:30 UT, while panels (b1)–(b4) provide the corresponding LASCO-C2 and LASCO-C3 views. In panel (b2), the low-coronal AIA 131 Å image is composite-overlaid with the LASCO-C2 FOV. Two segments are explicitly marked, namely the linear extension of the low-coronal eruption slit (S0 as shown in Figure 1b) and the manually measured apparent direction of the CME core (red dashed line). A clear projected angular separation of $10^\circ \pm 2.24^\circ$ is measured between them, where the uncertainty was determined by propagating the uncertainties of these two segments. Although the large separation between SolO and Earth provides a valuable stereoscopic perspective, the EUI observations do not allow a reliable three-dimensional (3D) reconstruction of the CME propagation axis. The $10^\circ$ offset indicates a change in the projected propagation direction of the erupting structure between the low corona and outer corona. It may be caused by true non-radial CME motion, 3D rotation of the erupting flux rope, or projection effects.

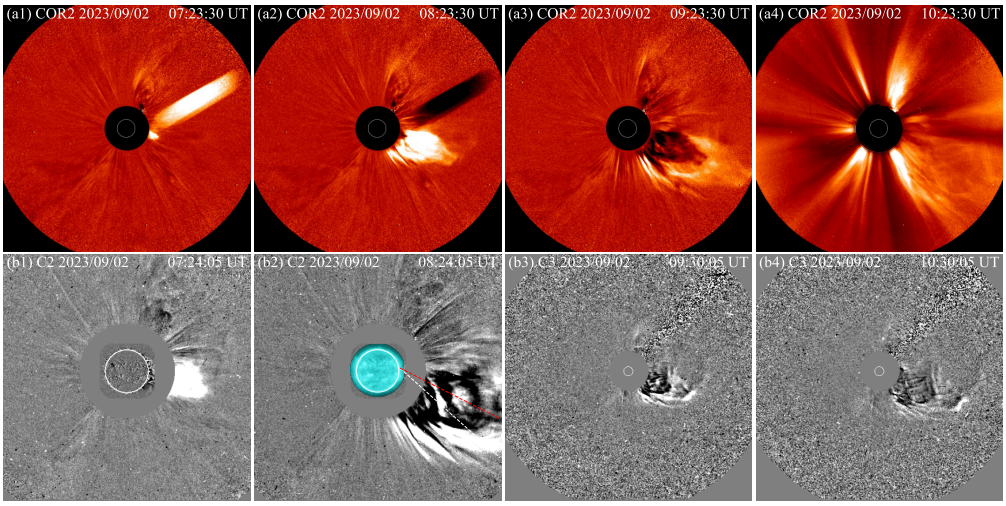



**Figure 6.** STEREO-A/COR2 (**a1**–**a4**), LASCO-C2 (**b1**,**b2**) and LASCO-C3 (**b3**,**b4**) observations showing the evolution of the associated CME. The AIA 131 Å image is overlaid on the LASCO-C2 FOV in panel (**b2**). The white dashed line marks the linear extension of the slit shown in Figure 1b, and the red dashed line marks the CME core propagation axis.

Numerous studies [44–46] have demonstrated that CME propagation and deflection trajectories at global scales ($1.1-2.5\ R_\odot$) are primarily governed by large-scale ambient magnetic pressure gradients and surrounding open/closed field topology, which PFSS models reasonably well. Hence, we analyzed the PFSS extrapolation of this event shown in Figure 7, illustrating the structural configuration at 06:04 UT from both the SDO viewpoint (Panel (a)) and the SolO viewpoint (Panel (b)). The model demonstrates a complex magnetic environment where open magnetic field lines (green lines) flank a massive complex of strong, asymmetric closed magnetic loops (white lines). The CME originated from the edge of the closed loop complex. The asymmetric distribution of these strong magnetic loops might produce a localized magnetic pressure gradient and/or asymmetric overlying tension, causing the erupting flux rope to deflect toward the neighboring weaker-field region, consistent with previous studies [47–50].

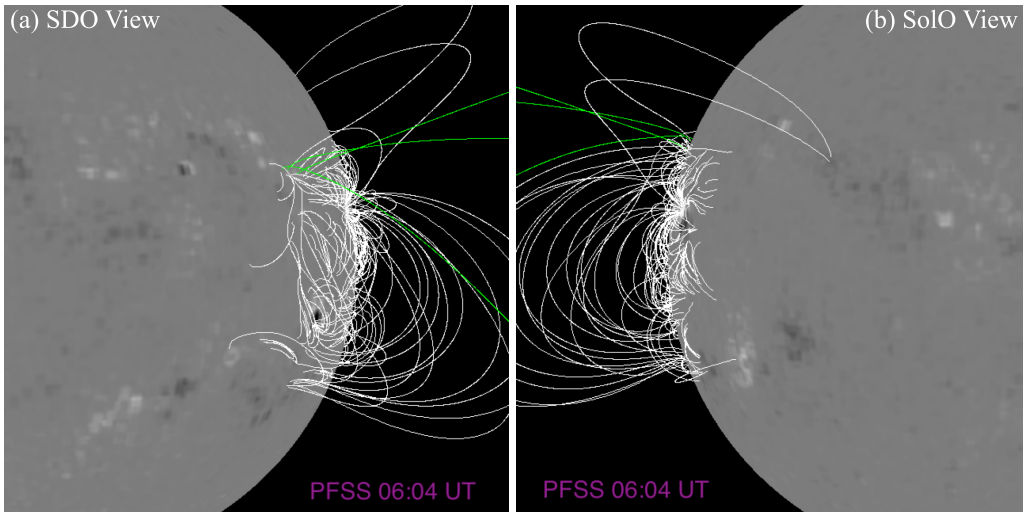



**Figure 7.** PFSS extrapolations from the SDO (**a**) and SolO (**b**) perspectives at 06:04 UT on 2 September 2023. The white lines indicate the closed magnetic field lines, and the green lines represent the open magnetic field lines.

Figure 8 plots the time–height evolution of the CME core within the FOV of LASCO-C2 and C3 (blue dots for C2 and cyan dots for C3, respectively). A linear regression fit to these data points (red dashed line) yields a nearly constant propagation speed of 519 km $s^{-1}$, which is comparable to the speed of the inner-coronal flux rope at 06:57:38 UT (501 km $s^{-1}$ as shown in Figure 4a). This agreement suggests that the CME had already completed the main acceleration phase below 2 $R_{\odot}$ and subsequently propagated at an approximately constant speed.

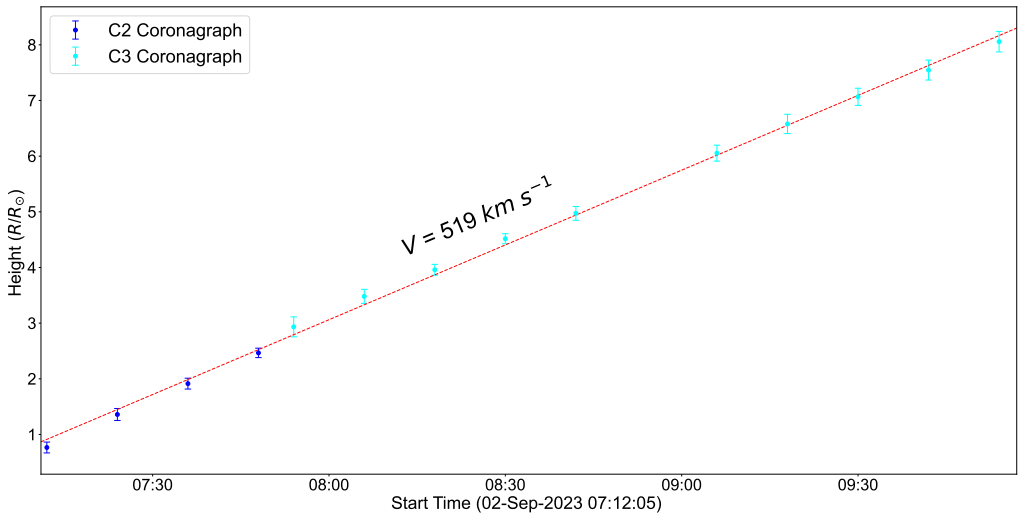



**Figure 8.** Height–time plot of the CME core observed by LASCO-C2 (blue dots) and LASCO-C3 (cyan dots), with vertical bars indicating height measurement errors. The result of a linear fit is overplotted with a dashed line and the speed (519 km $s^{-1}$) is labeled.

## 4. Discussion

### *4.1. The Piecewise Expansion of the Coronal Loops*

Unlike prior studies, in which the motion of the overlying magnetic envelope has generally been fitted by a single straight line or a smooth curve analogous to the trajectory of the flux rope [51–55], this work, to our knowledge, reveals a distinct kinematic mismatch for the first time. While the flux rope exhibits a characteristic initial slow ascent followed by rapid, abrupt acceleration (in agreement with classic eruption models [4–9]), the overlying

coronal loops demonstrate a piecewise linear trajectory rather than a continuously accelerating profile. Few observations have reported such clearly separated velocity regimes in coronal loop expansion during eruption.

The early slow-rise phase of the flux rope can be attributed to either tether-cutting reconnection beneath it [9], or continuous magnetic flux injection and footprint shearing/convergence at the photosphere [56–58], both of which force the rope to expand upward to maintain equilibrium. The subsequent rapid acceleration, meanwhile, is a possible signature of an ideal MHD instability, most notably the torus instability [59] or kink instability [60], triggered once the structure crosses a critical threshold.

In contrast, the overlying coronal loops display distinct, segmented velocity jumps (expanding sequentially at 7, 45, 101, and 320 km $s^{-1}$). Each discrete velocity jump (occurring at approximately 06:37:18 UT, 06:45:54 UT, and 06:54:09 UT) might correspond to an episode of magnetic reconnection that systematically opens or weakens a layer of the overlying magnetic cage as it is driven upward by the erupting flux rope [8]. When a restraining loop system undergoes reconnection, its downward magnetic tension abruptly drops. Then the loops suddenly experience a release in confinement and jump to a higher expansion velocity, manifesting as a sharp, piecewise linear change in the time–distance diagram. However, no clear localized brightenings or independent reconnection signatures were identified at these times for velocity jump. Therefore, episodic reconnection cannot be confirmed from current observations.

Alternatively, a relatively conservative yet more plausible explanation is LOS projection effects. Because the tracking slit integrates optically thin plasma emission along the view angle, it likely samples different nested magnetic shells sequentially [61–63]. As the underlying flux rope expands, it does not impact all overlying loops simultaneously; instead, it encounters, compresses, and accelerates distinct loop systems at progressively higher altitudes. In this scenario, each step change in velocity represents the tracking slit transitioning its primary intensity focus to a newly swept-up outer loop system.

### *4.2. The Oscillation of the Prominence*

The flux rope erupted along S0 shown in Figure 1b. The rapid lateral expansion was launched by the impulsive energy release and acted as a powerful mechanical piston directed toward the southern hemisphere until it impacted P1. In contrast, P2 was located in the northern hemisphere, completely behind the propagation axis of the erupting core, and thus could not be directly perturbed by the eruption. As a result, P2 exhibited no significant motion and remained relatively quiescent throughout the event, despite being spatially closer to the eruption source region.

P1 began to exhibit pronounced oscillations after 06:52:45 UT. Nearly identical oscillation periods were observed across all regions of the prominence as shown in Figure 5, indicating that the prominence underwent a global vertical oscillation of kink-like mode [64]. The model of Hyder [65] can be utilized to estimate the magnetic information of P1, wherein the prominence is treated as a damped harmonic oscillator moving through the surrounding solar corona. The restoring force is provided by the Lorentz force caused by the supporting magnetic field [29]. The observed decay of the oscillation amplitude is attributed to viscous friction between the prominence and the surrounding coronal plasma [24,66,67]:

$$B_r^2 = \pi \rho_p r_0^2 (4\pi^2 P^{-2} + \tau^{-2}). \quad (3)$$

Here, $B_r$ is the radial component of the prominence magnetic field, i.e., the component along the local solar-radial direction; $\rho_p$ is the prominence mass density; $r_0$ is the characteristic radial scale length describing the variation in $B_r$; P and $\tau$ are the period and damping

time scale of the oscillation, respectively. The prominence is treated as a lumped mass in Equation (3), so that the geometrical length of the prominence does not explicitly appear. The density of prominences typically ranges between $(1-10)\times10^{-14}$ g cm$^{-3}$ [68,69]. In our analysis, since $r_0$ cannot be reliably determined, the projected radial distance from the solar limb to the prominence center is adopted as an observational proxy, which is about $(0.82-1.03)\times10^9$ cm. The period and damping time were obtained using the weighted averaging method, yielding values of $517.71\pm5.14$ s and $1674.04\pm144.02$ s, respectively (see Table 3). The resulting model-dependent radial magnetic-field component $B_r$ is estimated to be 1.77–7.02 G. The uncertainties in P and $\tau$ contribute only a small uncertainty to $B_r$, whereas the adopted ranges of $\rho_p$ and $r_0$ dominate the uncertainty budget. The result is consistent with the values reported in previous papers [24,42,65,70,71].

Based on the above discussion, we present a schematic cartoon to illustrate the physical mechanism underlying this eruption event, as shown in Figure 9.

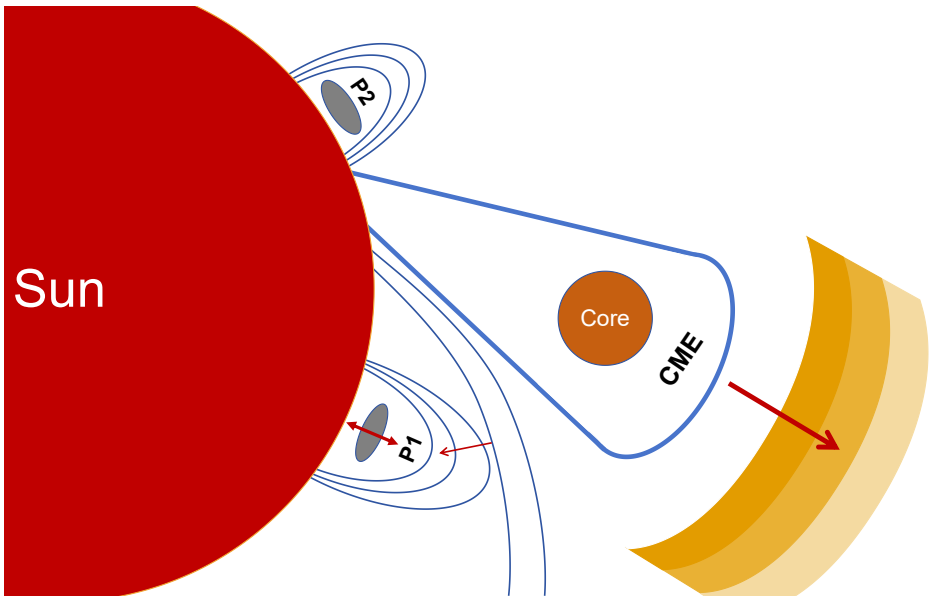



**Figure 9.** Qualitative schematic cartoon of the eruption event on 2 September 2023. Prominences P1 and P2 are indicated by two gray ellipses. The thin blue lines represent magnetic field lines. The thick blue lines and the regions they enclose correspond to the erupting material and associated magnetic field. The red arrows indicate the direction of motion of the objects they label. The layered structure in the lower-right corner signifies a possible mechanism of the piecewise motion of the overlying coronal loops, rather than representing a distinct layered loop configuration.

## 5. Summary

In this paper, we have carried out a comprehensive observational study of a solar eruptive event on 2 September 2023. The key findings are summarized below:

The event featured an energetic flare that peaked at about 07:00 UT, which was temporally consistent with the rapid acceleration of the flux rope from 42 km s$^{-1}$ to 501 km s$^{-1}$. The expansion of the flux rope drove a piecewise coronal loop expansion and generated a propagating disturbance. The CME maintained an approximately constant projected speed of 519 km s$^{-1}$ in interplanetary space, suggesting that the acceleration phase was completed entirely within $2R_\odot$.

The eruption-driven disturbance interacted with the prominence P1, triggering large-amplitude vertical oscillations ($A_0=1.22$ Mm, $P=517.71$ s, $\tau=1674.04$ s). For comparison, although prominence P2 was located closer to the eruption source region, it did not experience any significant disturbance or exhibit detectable oscillatory motions. Utiliz-

ing MHD seismology, we determined the local radial magnetic field strength of P1 to be 1.77−7.02 G.

**Supplementary Materials:** The following supporting information can be downloaded at: https://www.mdpi.com/article/10.3390/universe12100293/s1.

**Author Contributions:** Conceptualization, Q.Z. and Y.Z.; methodology, Y.Z.; software, Y.Z.; validation, Q.Z. and Y.Z.; formal analysis, Y.Z.; investigation, Y.Z.; resources, Q.Z.; data curation, Y.Z.; writing—original draft preparation, Y.Z.; writing—review and editing, Q.Z. and Y.Z.; visualization, Y.Z.; supervision, Q.Z.; project administration, Q.Z. and Y.Z.; funding acquisition, Q.Z. and Y.Z. All authors have read and agreed to the published version of the manuscript.

**Funding:** This research was funded by National Natural Science Foundation of China (NSFC, grant Nos. 12403068, 12373065); Natural Science Foundation of Jiangsu Province (BK20241707).

**Data Availability Statement:** The dataset will be provided upon request.

**Acknowledgments:** The authors are grateful to the colleagues in Purple Mountain Observatory for their constructive suggestions and comments. SDO is a mission of NASA's Living With a Star Program. SolO is a mission of ESA with contributions from NASA and other international partners. SOHO is a cooperative ESA–NASA spacecraft. STEREO is a mission of NASA's Solar Terrestrial Probes program.

**Conflicts of Interest:** The authors declare no conflicts of interest.

## References

1. Forbes, T.G. A review on the genesis of coronal mass ejections. *J. Geophys. Res.* **2000**, *105*, 23153–23166. [CrossRef]
2. Webb, D.F.; Howard, T.A. Coronal Mass Ejections: Observations. *Living Rev. Sol. Phys.* **2012**, *9*, 3. [CrossRef]
3. Al-Haddad, N.; Lugaz, N. The Magnetic Field Structure of Coronal Mass Ejections: A More Realistic Representation. *Space Sci. Rev.* **2025**, *221*, 12. [CrossRef]
4. Carmichael, H. A Process for Flares. In *NASA Special Publication*; Hess, W.N., Ed.; NASA: Washington, DC, USA, 1964; Volume 50, p. 451.
5. Sturrock, P.A. Model of the High-Energy Phase of Solar Flares. *Nature* **1966**, *211*, 695–697. [CrossRef]
6. Hirayama, T. Theoretical Model of Flares and Prominences. I: Evaporating Flare Model. *Sol. Phys.* **1974**, *34*, 323–338. [CrossRef]
7. Kopp, R.A.; Pneuman, G.W. Magnetic reconnection in the corona and the loop prominence phenomenon. *Sol. Phys.* **1976**, *50*, 85–98. [CrossRef]
8. Antiochos, S.K.; DeVore, C.R.; Klimchuk, J.A. A Model for Solar Coronal Mass Ejections. *Astrophys. J.* **1999**, *510*, 485–493. [CrossRef]
9. Moore, R.L.; Sterling, A.C.; Hudson, H.S.; Lemen, J.R. Onset of the Magnetic Explosion in Solar Flares and Coronal Mass Ejections. *Astrophys. J.* **2001**, *552*, 833–848. [CrossRef]
10. Cheng, X.; Zhang, J.; Liu, Y.; Ding, M.D. Observing Flux Rope Formation During the Impulsive Phase of a Solar Eruption. *Astrophys. J. Lett.* **2011**, *732*, L25. [CrossRef]
11. Zhang, J.; Cheng, X.; Ding, M.D. Observation of an evolving magnetic flux rope before and during a solar eruption. *Nat. Commun.* **2012**, *3*, 747. [CrossRef] [PubMed]
12. Jiang, C.; Feng, X.; Liu, R.; Yan, X.; Hu, Q.; Moore, R.L.; Duan, A.; Cui, J.; Zuo, P.; Wang, Y.; et al. A fundamental mechanism of solar eruption initiation. *Nat. Astron.* **2021**, *5*, 1126–1138. [CrossRef]
13. Pontin, D.I.; Priest, E.R. Magnetic reconnection: MHD theory and modelling. *Living Rev. Sol. Phys.* **2022**, *19*, 1. [CrossRef]
14. Gary, D.E. New Insights from Imaging Spectroscopy of Solar Radio Emission. *Annu. Rev. Astron. Astrophys.* **2023**, *61*, 427–472. [CrossRef]
15. Thompson, B.J.; Plunkett, S.P.; Gurman, J.B.; Newmark, J.S.; St. Cyr, O.C.; Michels, D.J. SOHO/EIT observations of an Earth-directed coronal mass ejection on May 12, 1997. *Geophys. Res. Lett.* **1998**, *25*, 2465–2468. [CrossRef]
16. Wills-Davey, M.J.; Attrill, G.D.R. EIT Waves: A Changing Understanding over a Solar Cycle. *Space Sci. Rev.* **2009**, *149*, 325–353. [CrossRef]
17. Warmuth, A. Large-scale globally propagating coronal waves. *Living Rev. Sol. Phys.* **2015**, *12*, 3. [CrossRef]
18. Olmedo, O.; Vourlidas, A.; Zhang, J.; Cheng, X. Secondary Waves and/or the "Reflection" from and "Transmission" through a Coronal Hole of an Extreme Ultraviolet Wave Associated with the 2011 February 15 X2.2 Flare Observed with SDO/AIA and STEREO/EUVI. *Astrophys. J.* **2012**, *756*, 143. [CrossRef]

19. Chen, P.F.; Wu, Y. First Evidence of Coexisting EIT Wave and Coronal Moreton Wave from SDO/AIA Observations. *Astrophys. J. Lett.* **2011**, *732*, L20. [CrossRef]
20. Veronig, A.M.; Muhr, N.; Kienreich, I.W.; Temmer, M.; Vršnak, B. First Observations of a Dome-shaped Large-scale Coronal Extreme-ultraviolet Wave. *Astrophys. J. Lett.* **2010**, *716*, L57–L62. [CrossRef]
21. Chen, P.F.; Fang, C.; Shibata, K. A Full View of EIT Waves. *Astrophys. J.* **2005**, *622*, 1202–1210. [CrossRef]
22. Liu, W.; Nitta, N.V.; Schrijver, C.J.; Title, A.M.; Tarbell, T.D. First SDO AIA Observations of a Global Coronal EUV "Wave": Multiple Components and "Ripples". *Astrophys. J. Lett.* **2010**, *723*, L53–L59. [CrossRef]
23. Isobe, H.; Tripathi, D. Large amplitude oscillation of a polar crown filament in the pre-eruption phase. *Astron. Astrophys.* **2006**, *449*, L17–L20. [CrossRef]
24. Zhang, Q.M.; Ji, H.S. Vertical Oscillation of a Coronal Cavity Triggered by an EUV Wave. *Astrophys. J.* **2018**, *860*, 113. [CrossRef]
25. Hershaw, J.; Foullon, C.; Nakariakov, V.M.; Verwichte, E. Damped large amplitude transverse oscillations in an EUV solar prominence, triggered by large-scale transient coronal waves. *Astron. Astrophys.* **2011**, *531*, A53. [CrossRef]
26. Dai, J.; Zhang, Q.; Zhang, Y.; Xu, Z.; Su, Y.; Ji, H. Oscillations and Mass Draining that Lead to a Sympathetic Eruption of a Quiescent Filament. *Astrophys. J.* **2021**, *923*, 74. [CrossRef]
27. Liakh, V.; Luna, M.; Khomenko, E. Numerical simulations of prominence oscillations triggered by external perturbations. *Astron. Astrophys.* **2023**, *673*, A154. [CrossRef]
28. Liakh, V.; Keppens, R. Numerical study of solar eruption, extreme-ultraviolet wave propagation, and wave-induced prominence dynamics. *Astron. Astrophys.* **2025**, *696*, A158. [CrossRef]
29. Chen, J.; Schuck, P.W. Damped Oscillations of Coronal Loops. *Sol. Phys.* **2007**, *246*, 145–164. [CrossRef]
30. Kim, S.; Nakariakov, V.M.; Cho, K.S. Vertical Kink Oscillation of a Magnetic Flux Rope Structure in the Solar Corona. *Astrophys. J. Lett.* **2014**, *797*, L22. [CrossRef]
31. Arregui, I.; Oliver, R.; Ballester, J.L. Prominence oscillations. *Living Rev. Sol. Phys.* **2018**, *15*, 3. [CrossRef]
32. Luna, M.; Karpen, J. Large-amplitude Longitudinal Oscillations in a Solar Filament. *Astrophys. J. Lett.* **2012**, *750*, L1. [CrossRef]
33. Lemen, J.R.; Title, A.M.; Akin, D.J.; Boerner, P.F.; Chou, C.; Drake, J.F.; Duncan, D.W.; Edwards, C.G.; Friedlaender, F.M.; Heyman, G.F.; et al. The Atmospheric Imaging Assembly (AIA) on the Solar Dynamics Observatory (SDO). *Sol. Phys.* **2012**, *275*, 17–40. [CrossRef]
34. Pesnell, W.D.; Thompson, B.J.; Chamberlin, P.C. The Solar Dynamics Observatory (SDO). *Sol. Phys.* **2012**, *275*, 3–15. [CrossRef]
35. Müller, D.; St. Cyr, O.C.; Zouganelis, I.; Gilbert, H.R.; Marsden, R.; Nieves-Chinchilla, T.; Antonucci, E.; Auchère, F.; Berghmans, D.; Horbury, T.S.; et al. The Solar Orbiter mission. Science overview. *Astron. Astrophys.* **2020**, *642*, A1. [CrossRef]
36. Krucker, S.; Hurford, G.J.; Grimm, O.; Kögl, S.; Gröbelbauer, H.P.; Etesi, L.; Casadei, D.; Csillaghy, A.; Benz, A.O.; Arnold, N.G.; et al. The Spectrometer/Telescope for Imaging X-rays (STIX). *Astron. Astrophys.* **2020**, *642*, A15. [CrossRef]
37. Rochus, P.; Auchère, F.; Berghmans, D.; Harra, L.; Schmutz, W.; Schühle, U.; Addison, P.; Appourchaux, T.; Aznar Cuadrado, R.; Baker, D.; et al. The Solar Orbiter EUI instrument: The Extreme Ultraviolet Imager. *Astron. Astrophys.* **2020**, *642*, A8. [CrossRef]
38. Brueckner, G.E.; Howard, R.A.; Koomen, M.J.; Korendyke, C.M.; Michels, D.J.; Moses, J.D.; Socker, D.G.; Dere, K.P.; Lamy, P.L.; Llebaria, A.; et al. The Large Angle Spectroscopic Coronagraph (LASCO). *Sol. Phys.* **1995**, *162*, 357–402. [CrossRef]
39. Howard, R.A.; Moses, J.D.; Vourlidas, A.; Newmark, J.S.; Socker, D.G.; Plunkett, S.P.; Korendyke, C.M.; Cook, J.W.; Hurley, A.; Davila, J.M.; et al. Sun Earth Connection Coronal and Heliospheric Investigation (SECCHI). *Space Sci. Rev.* **2008**, *136*, 67–115. [CrossRef]
40. Zhang, Q.; Li, C.; Li, D.; Qiu, Y.; Zhang, Y.; Ni, Y. First Detection of Transverse Vertical Oscillation during the Expansion of Coronal Loops. *Astrophys. J. Lett.* **2022**, *937*, L21. [CrossRef]
41. Bocchialini, K.; Baudin, F.; Koutchmy, S.; Pouget, G.; Solomon, J. Oscillatory motions observed in eruptive filaments. *Astron. Astrophys.* **2011**, *533*, A96. [CrossRef]
42. Shen, Y.; Ichimoto, K.; Ishii, T.T.; Tian, Z.; Zhao, R.; Shibata, K. A Chain of Winking (Oscillating) Filaments Triggered by an Invisible Extreme-ultraviolet Wave. *Astrophys. J.* **2014**, *786*, 151. [CrossRef]
43. Zhang, Y.; Zhang, Q.; Song, D.c.; Ji, H. Transverse Oscillation of Prominence and Filament Induced by an Extreme-ultraviolet Wave from the Far Side of the Sun. *Astrophys. J.* **2024**, *963*, 140. [CrossRef]
44. Gui, B.; Shen, C.; Wang, Y.; Ye, P.; Liu, J.; Wang, S.; Zhao, X. Quantitative Analysis of CME Deflections in the Corona. *Sol. Phys.* **2011**, *271*, 111–139. [CrossRef]
45. Kay, C.; Opher, M.; Evans, R.M. Global Trends of CME Deflections Based on CME and Solar Parameters. *Astrophys. J.* **2015**, *805*, 168. [CrossRef]
46. Sieyra, M.V.; Cécere, M.; Cremades, H.; Iglesias, F.A.; Sahade, A.; Mierla, M.; Stenborg, G.; Costa, A.; West, M.J.; D'Huys, E. Analysis of Large Deflections of Prominence-CME Events during the Rising Phase of Solar Cycle 24. *Sol. Phys.* **2020**, *295*, 126. [CrossRef]
47. Thernisien, A.F.R.; Howard, R.A.; Vourlidas, A. Modeling of Flux Rope Coronal Mass Ejections. *Astrophys. J.* **2006**, *652*, 763–773. [CrossRef] [PubMed]

48. Möstl, C.; Rollett, T.; Frahm, R.A.; Liu, Y.D.; Long, D.M.; Colaninno, R.C.; Reiss, M.A.; Temmer, M.; Farrugia, C.J.; Posner, A.; et al. Strong coronal channelling and interplanetary evolution of a solar storm up to Earth and Mars. *Nat. Commun.* **2015**, *6*, 7135. [CrossRef] [PubMed]
49. Kay, C.; Gopalswamy, N.; Xie, H.; Yashiro, S. Deflection and Rotation of CMEs from Active Region 11158. *Sol. Phys.* **2017**, *292*, 78. [CrossRef] [PubMed]
50. Cécere, M.; Costa, A.; Cremades, H.; Stenborg, G. Recent insights on CME deflections at low heights. *Front. Astron. Space Sci.* **2023**, *10*, 1260432. [CrossRef]
51. Kumar, P.; Cho, K.S. Multiwavelength observation of a large-scale flux rope eruption above a kinked small filament. *Astron. Astrophys.* **2014**, *572*, A83. [CrossRef]
52. Su, Y.; van Ballegooijen, A.; McCauley, P.; Ji, H.; Reeves, K.K.; DeLuca, E.E. Magnetic Structure and Dynamics of the Erupting Solar Polar Crown Prominence on 2012 March 12. *Astrophys. J.* **2015**, *807*, 144. [CrossRef]
53. Zhang, Q.M.; Su, Y.N.; Ji, H.S. Pre-flare coronal dimmings. *Astron. Astrophys.* **2017**, *598*, A3. [CrossRef]
54. Zhang, Q.M.; Chen, J.L.; Li, S.T.; Lu, L.; Li, D. Transverse Coronal-Loop Oscillations Induced by the Non-radial Eruption of a Magnetic Flux Rope. *Sol. Phys.* **2022**, *297*, 18. [CrossRef]
55. Cheng, X.; Xing, C.; Aulanier, G.; Solanki, S.K.; Peter, H.; Ding, M.D. Deciphering the Slow-rise Precursor of a Major Coronal Mass Ejection. *Astrophys. J. Lett.* **2023**, *954*, L47. [CrossRef]
56. van Ballegooijen, A.A.; Martens, P.C.H. Formation and Eruption of Solar Prominences. *Astrophys. J.* **1989**, *343*, 971. [CrossRef] [PubMed]
57. Chen, J. Theory of prominence eruption and propagation: Interplanetary consequences. *J. Geophys. Res.* **1996**, *101*, 27499–27520. [CrossRef]
58. Zhang, Y.; Xu, Z.; Zhang, Q.; Dai, J.; Ji, H. Sunspot Shearing and Sudden Retraction Motion Associated with the 2013 August 17 M3.3 Flare. *Astrophys. J. Lett.* **2022**, *933*, L20. [CrossRef]
59. Kliem, B.; Török, T. Torus Instability. *Phys. Rev. Lett.* **2006**, *96*, 255002. [CrossRef] [PubMed]
60. Hood, A.W.; Priest, E.R. Kink Instability of Solar Coronal Loops as the Cause of Solar Flares. *Sol. Phys.* **1979**, *64*, 303–321. [CrossRef]
61. O'Dwyer, B.; Del Zanna, G.; Mason, H.E.; Weber, M.A.; Tripathi, D. SDO/AIA response to coronal hole, quiet Sun, active region, and flare plasma. *Astron. Astrophys.* **2010**, *521*, A21. [CrossRef]
62. Pagano, P.; Mackay, D.H.; Poedts, S. Simulating AIA observations of a flux rope ejection. *Astron. Astrophys.* **2014**, *568*, A120. [CrossRef]
63. Liu, R. Magnetic flux ropes in the solar corona: Structure and evolution toward eruption. *Res. Astron. Astrophys.* **2020**, *20*, 165. [CrossRef]
64. Zhou, G.P.; Zhang, J.; Wang, J.X. Observations of Magnetic Flux-rope Oscillation during the Precursor Phase of a Solar Eruption. *Astrophys. J. Lett.* **2016**, *823*, L19. [CrossRef]
65. Hyder, C.L. Winking Filaments and Prominence and Coronal Magnetic Fields. *Z. Für Astrophys.* **1966**, *63*, 78.
66. Díaz, A.J.; Oliver, R.; Erdélyi, R.; Ballester, J.L. Fast MHD oscillations in prominence fine structures. *Astron. Astrophys.* **2001**, *379*, 1083–1097. [CrossRef]
67. Zhou, Y.H.; Xia, C.; Keppens, R.; Fang, C.; Chen, P.F. Three-dimensional MHD Simulations of Solar Prominence Oscillations in a Magnetic Flux Rope. *Astrophys. J.* **2018**, *856*, 179. [CrossRef]
68. Parenti, S. Solar Prominences: Observations. *Living Rev. Sol. Phys.* **2014**, *11*, 1. [CrossRef]
69. Labrosse, N.; Heinzel, P.; Vial, J.C.; Kucera, T.; Parenti, S.; Gunár, S.; Schmieder, B.; Kilper, G. Physics of Solar Prominences: I—Spectral Diagnostics and Non-LTE Modelling. *Space Sci. Rev.* **2010**, *151*, 243–332. [CrossRef]
70. Shen, Y.; Liu, Y.; Tian, Z.; Qu, Z. On a Small-scale EUV Wave: The Driving Mechanism and the Associated Oscillating Filament. *Astrophys. J.* **2017**, *851*, 101. [CrossRef]
71. Dai, J.; Zhang, Q.; Qiu, Y.; Li, C.; Li, Z.; Li, S.; Su, Y.; Ji, H. Simultaneous Horizontal and Vertical Oscillation of a Quiescent Filament Observed by CHASE and SDO. *Astrophys. J.* **2023**, *959*, 71. [CrossRef]


**Disclaimer/Publisher's Note:** The statements, opinions and data contained in all publications are solely those of the individual author(s) and contributor(s) and not of MDPI and/or the editor(s). MDPI and/or the editor(s) disclaim responsibility for any injury to people or property resulting from any ideas, methods, instructions or products referred to in the content.